



Fresh state and hydration properties of high-volume lithium slag cement composites

S M Arifur Rahman · Aziz Hasan Mahmood · Faiz Uddin Ahmed Shaikh  · Prabir Kumar Sarker

Received: 10 November 2022 / Accepted: 13 April 2023 / Published online: 11 May 2023
© The Author(s) 2023

Abstract In this study, the fresh state and hydration properties of 0–60% lithium slag blended cement pastes were investigated at water-binder ratio of 0.47. The workability of the fresh pastes was evaluated by measuring the air content, marsh cone flow, mini-slump flow, setting times, and through rheology tests. A 40% lithium slag cement could produce 91% strength activity index at 28 days; mini-slump pat diameter of 70.54 mm; marsh cone flow efflux time of 145 s; air content 0.6%; hydration heat of 300 J/g (at 72 h). At replacement levels above 40%, the strength activity index, air content, mini-slump flow, hydration heat, and fluidity were significantly reduced. Experimental investigations confirm that the mini-slump test provides the best correlation coefficients ($R^2 = 0.96$) with the maximum shear viscosity of lithium slag cement pastes than the marsh cone flow efflux time and air content. The classical slump and rheological models were used to characterise the mini-slump, yield stress, and plastic viscosity of low to high volume lithium slag cement pastes. The present study recommends that a 40% lithium slag cement paste is a

viable option to produce green concrete for optimum fresh, hydration, rheological, and hardened properties.

Keywords Lithium slag · Fresh properties · Hydration · Rheology · Mini-slump · Slump models · Rheology models

1 Introduction

Cement is the most popular and traditional concrete binder for concrete, and its production is the third largest carbon footprint emitter [1]. Currently, researchers are studying the reaction mechanisms of supplementary cementitious materials (SCM) in conjunction with cement to produce low-carbon concrete and reduce the overall concrete carbon footprint. The commonly used SCMs are fly ash, blast furnace slag, kaolin, natural pozzolans, and silica fume, and their characterisation and performance have been measured through the specified standard procedure [2, 3]. With a shift in power plants from generating electricity from coal towards sustainable fuel sources, there is a steady decline in fly ash production and other SCMs are not readily available globally. As such, alternative SCMs must be investigated to determine their potential to be used in concrete manufacture. A potential alternative to traditional SCMs can be lithium slag, particularly for Australia, which is the world's largest lithium producer accounting for 54% of global lithium

SMA. Rahman · F. U. A. Shaikh (✉) · P. K. Sarker
Department of Civil Engineering, School of Civil and Mechanical Engineering, Curtin University, Perth, Australia
e-mail: shaikhfa@rocketmail.com

A. H. Mahmood
School of Civil and Environmental Engineering,
University of New South Wales, Sydney, Australia



production in 2019 [1] and houses the largest production mine (Greenbushes) [4]. In general, the physical and chemical compositions of lithium slag are beneficial as a SCM to produce green concrete. Several research reported that the specific surface area and median particle size of lithium slag are not only found suitable for partial replacement of cement but most importantly, high proportion of SiO_2 , Al_2O_3 , and CaO could induce pozzolanic activity [5–13].

Researchers used low-volume lithium slag as SCM in concrete in the past and demonstrated adequate strength, durability, and microstructure improvement in line with other pozzolans [5–12, 14–16]. However, these studies are trial based towards establishing an optimum mix proportion leaving an opportunity for understanding lithium slag's impact on concrete fresh state properties. Thus, it is highly desirable to investigate the optimum lithium slag cement pastes till the mixture's fresh properties remain compatible with workability.

Researchers preliminary investigated the fresh properties of lithium slag cement pastes, and the tests include setting times, air content, hydration heat, fresh density, and fluidity at 10–30% cement replacement with lithium slag [13]. Previous studies reported that the lithium slag in cement pastes increased the setting times and reduced the air content [17, 18]. Haigh et al. [17] and Munn et al. [18] discussed the setting times of lithium slag as a SCM. Haigh et al. used 25% lithium slag as a SCM for the production of 25 and 40 MPa concretes. The study used 1.44 and 1.56% high range water reducing admixture to maintain the design slump (100 mm) for each of the mixes. The initial/final settings times of 25% LS contained 25 and 40 MPa concretes were 580/690 and 570/690 min, respectively. In the same comparison, the initial/final setting times of the control were 290/400 and 320/420 min, respectively. The study concluded that high percentage of water reducing admixture prolonged the setting times of lithium slag concrete. Later, Munn et al. used 25% calcined and 25% non-calcined lithium slag as a SCM for the production of concrete. For both mixes the initial/final setting times were very close to the 25% fly ash as the control concrete (365/460 min). The study concluded that addition of 25% lithium slag as a SCM did not produce any significant difference in setting times. On the other hand, Haigh et al. [17] also reported that the air content of both control and 25% lithium slag cement pastes was 2%, while Munn et al.

[18] found that the air content was increased by 0.5% in the same comparison. The study on the setting times and air content due to the addition of lithium slag as a SCM was not reflected in previous studies, thus in this study the number of original control groups were increased to understand how the setting times and air content are changed due to 0–60% cement replacement by lithium slag.

Later, researchers used chemical activators like triisopropanolamine [9] and triethanolamine [12] to induce the pozzolanic reaction of SCMs. These alkanolamines can maintain higher alkaline medium to promote the ion dissolution in the system [19] and expediate the hydration of cement by bonding itself with ferric and aluminate phases [20]. Also, He et al. [12] proposed the rheological behaviour of triethanolamine (0.1–0.2% binder weight) containing 20% lithium slag cement paste with water-binder ratio (w/b) of 0.50 and fitted with the Herschel-Bulkley model [21]. The scope of the study was limited to calculating the flow behaviour index of lithium slag cement pastes based on the experimental shear stress. In a separate study, Zhang et al. [9] investigated the hydration characteristics of triisopropanolamine (0.06–0.10% of binder weight) added 30% lithium slag cement paste with w/b = 0.38 and characterised the secondary hydration peak due to addition of high-volume lithium slag. Tan et al. [8] also characterised the secondary hydration peak of 2.5–10% lithium slag cement pastes induced during the conversion of ettringite (AFt) to secondary ettringite (AFm). Furthermore, He et al. [22] investigated the mechanical properties of cement concrete incorporating 10–30% lithium slag. The study found that a 75% strength activity index at 28 days can be achieved when 30% lithium slag is used as SCM in concrete. Previous studies have successfully enhanced the hydration, rheological, and pozzolanic properties of 10–30% lithium slag cement composites by incorporating chemical activators. It would be interesting to explore the potential of lithium slag as a SCM without the use of activators to determine its properties in this regard.

The present study conducted a meticulous experimental analysis to determine the air content, efflux time, mini-slump, heat of hydration, and rheology of 0–60% lithium slag cement pastes. To estimate the yield stress and plastic viscosity of fresh pastes, classical rheology models [21, 23–26] were meticulously employed. The accuracy of the rheology models



was then determined using the standard error by comparing the experimental data with analytically predicted data. To further evaluate the workability of lithium slag cement pastes, the experimentally determined slump flow and yield stress data were transformed into a dimensionless form and compared with classical slump models [27–31]. This method provided a precise and robust characterisation of the paste's workability. In summary, this study was motivated by the goal of optimising the use of lithium slag as a SCM for the production of low-carbon concrete through high-volume cement substitutions. By enhancing workability, strength, and hydration properties in comparison to the control mix, this research contributes to the paradigm understanding of using high-volume lithium slag cement composites. The results of this study will facilitate the development of sustainable and environmentally friendly construction materials, ensuring the long-term viability of the industry.

2 Materials

The metal oxides composition and loss on ignition (LOI) of Ordinary Portland Cement and ground lithium slag were evaluated using X-ray fluorescence (XRF) analysis, and the results are provided in Table 1. The in-situ water content of lithium slag was 28.3%. Primarily, the lithium slag was dried at 105 ± 5 °C and ground in a ball mill for 10 min to break the lumps. The Blaine specific surface area of cement and lithium slag were 360 kg/m^2 and 342 kg/m^2 , respectively. Also, the grain size distribution of cement and lithium slag are shown in Fig. 1a, and the median particle size of cement and lithium slag was found to be 17 and 38 μm , respectively. In addition, the specific gravity of cement and lithium slag were 3.1 and 2.46, respectively. The particles of lithium slag were irregular-shaped (flaky and angular) and a combination of smooth and rough textures, along with some

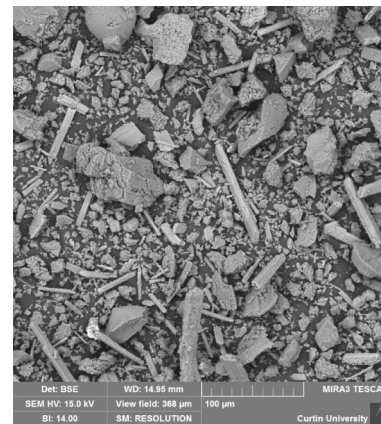
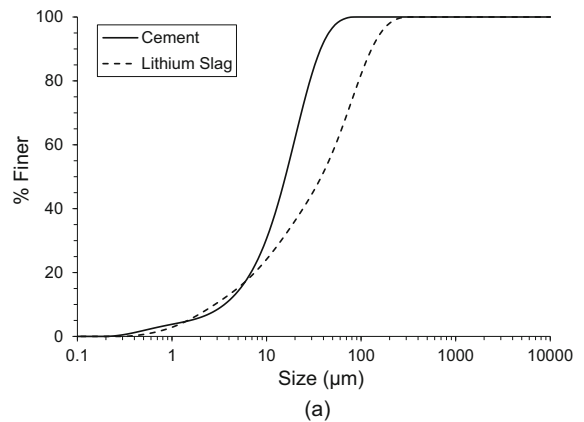


Fig. 1 Grain size distribution of cement and lithium slag (a), and b particle morphology of lithium slag under scanning electron microscope

flaky particles as observed in a scanning electron microscope (SEM) and shown in Fig. 1b.

3 Experimental methodology

The fresh properties of cement pastes containing 0–60% lithium slag, such as, mini-slump flow, marsh cone flow, air content, consistency, and setting time etc. are investigated in this study. The heat of

Table 1 Oxide content of cement and grinded lithium slag (in mass percentage)

Materials	SiO ₂	Al ₂ O ₃	Fe ₂ O ₃	CaO	MgO	SO ₃	K ₂ O	Na ₂ O	LOI
Cement	20.70	5.70	2.90	63.10	1.30	3.30	0.40	0.30	1.90
Lithium slag	54.60	21.10	1.50	7.50	0.60	5.60	0.90	0.70	6.70

hydration and rheological features of the pastes were also monitored to understand the role of lithium slag on such properties. Prior to investigations, pastes were formulated using a generalised mixing procedure of the binders (cement and pozzolan) and water as shown in Fig. 2. The formulations of the paste specimens are outlined in Table 2.

The dry binders were mechanically mixed while for preparing the paste specimens, the dry binders were weighted and mixed in low shear for 3 min to homogenize the system. Water was then added to the homogeneous blend and the wet mix was continued for a further 60 s while hand-scraped and stirred from the bottom and side walls of the bowl continuously. A consecutive low and medium shear mixing was imposed after every 60 s by the Hobert mixer. The total wet mixing duration was 8 min.

The optimum w/b of the cement-lithium slag composite was determined from the mini-slump cone

Table 2 Mix design for different fresh and hardened tests

Mix IDs	Cement (%)	Lithium slag (%)	w/b
Control	100	–	0.47
10% LS	90	10	0.47
20% LS	80	20	0.47
30% LS	70	30	0.47
40% LS	60	40	0.47
50% LS	50	50	0.47
60% LS	40	60	0.47

[32], air content [33], and marsh flow cone [34] tests and listed in Table 2. The top and bottom diameters of mini-slump cone are 19 and 38 mm, respectively, and the height is 57 mm. The cone was filled from the top in three layers, and a 2 mm diameter tamping rod was used to free fall 25 times in each layer from the surface

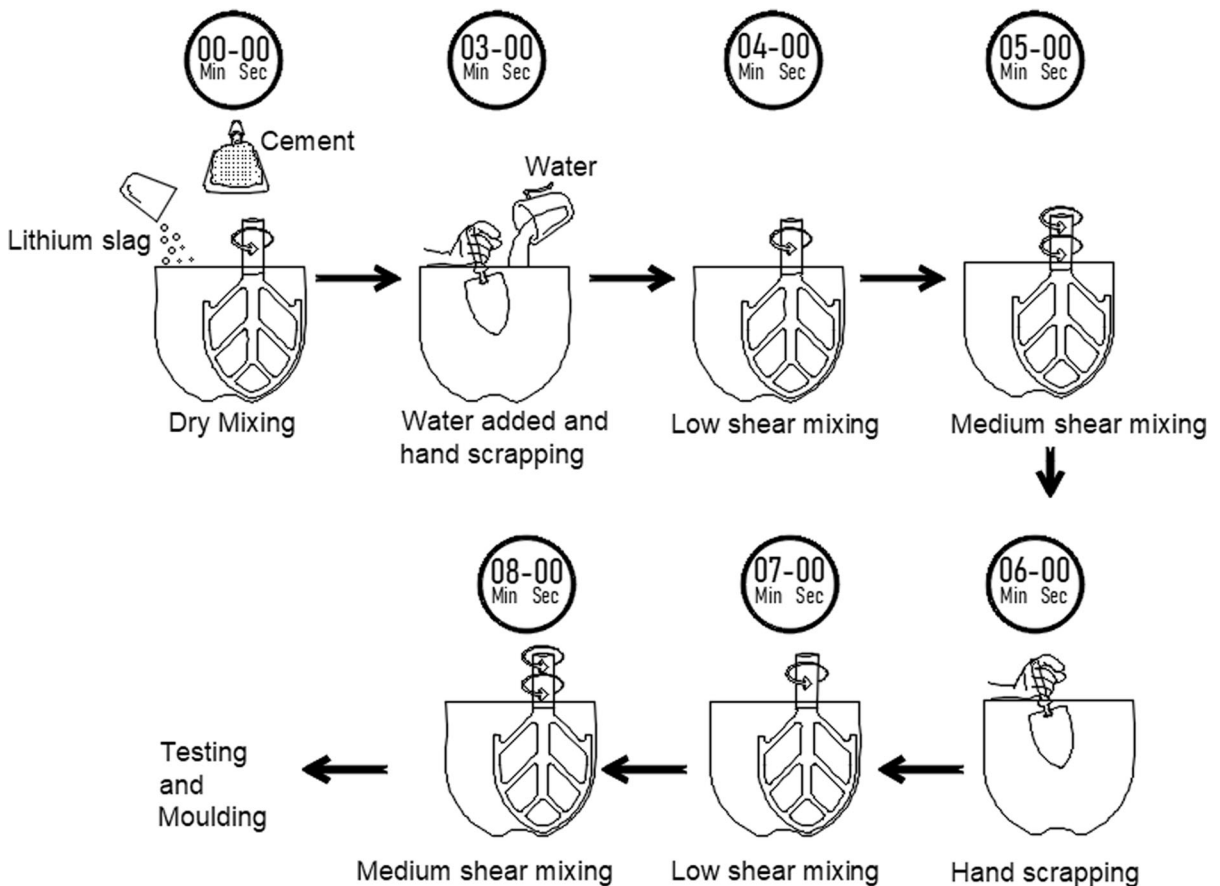


Fig. 2 Mixing procedure of the samples



to compact the paste. Then, the cone was lifted upward with approximately 1 mm/second to reduce the paste disturbance from cone wall contact. Also, the efflux time was measured by the marsh cone, which allows flowing 1725 mL of freshly prepared pastes through 12.7 mm diameter nozzle under gravity. Later, the freshly prepared paste was poured in the air content measuring mould in three layers and each layer was compacted for 25 times with a 25 mm tamping rod.

Water consistency [35] and setting times [36] were tested for each mix, and the w/b ratio of all mixes was based on the water consistency. The freshly prepared paste of each batch was then tested for air content [37]. The changes in the heat of hydration of cement from partial replacements by lithium slag were investigated by capturing the heat evolution in a TAM Air isothermal calorimeter. A 6-g hand-mixed paste sample was taken into an ampoule and loaded into the calorimeter at 40 °C to induce the pozzolanic activity of LS. The heat of hydration in the first 72 h was continually measured. Each test was repeated twice, and similar results were obtained. The average of the results is reported hereafter.

Later, the rheology of the 0–60% lithium slag cement pastes was tested by a Malvern DSR KINEXUS rheometer. A parallel plate (25 mm diameter) geometry with a 1.05 mm gap was adopted for all fresh mixes with an increasing shear rate from zero to 200 s⁻¹ within 180 s at 23 °C [38]. All the fresh mixes were allowed to delay by 300 s to reach the steady state and constant temperature after placing on the bottom plate of the geometry. The total testing time was 480 s for each mix. The shear stresses with increasing shear rate were recorded for all mixes within 5% steady state tolerance specified by the manufacturer. Finally, the compressive strength [39] of wet cured 50 mm cube paste specimens was determined at 7, 28, 56, and 180 days for all mixes. Fresh pastes were poured and compacted in cubical acrylic moulds on a vibrating table and left undisturbed for 24 h before stripping them off the moulds. The specimens were then cured in a lime-saturated water bath set at 23 °C until the age of testing as per AS 1012.8 [40] guidelines.

4 Mathematical models

4.1 Rheology models

The cement paste rheology depends on the grain size and shape, water content, temperature, and hydration [41]. Generally, the rheological properties are highly influenced in a composite fresh mix and the major factors are size and shape of SCMs used, volume contribution, and w/b ratio. The rheological behaviour of fresh cement paste is similar to the non-Newtonian fluid and several hypothetical models were developed for the idealisation of yield stress and plastic viscosity from experimental shear stress versus shear rate. The Bingham [23], modified Bingham [24], Herschel-Bulkley [21], Bingham-Papanastasiou [25], and Casson [26] models are commonly used for the idealisation of fresh cement pastes, and the shear stress can be predicted by the Eqs. 1–5.

$$\text{Bingham model } \tau = \tau_0 + \mu\dot{\gamma} \quad (1)$$

$$\text{Modified Bingham model } \tau = \tau_0 + \mu\dot{\gamma} + c\dot{\gamma}^2 \quad (2)$$

$$\text{Herschel – Bulkley model } \tau = \tau_0 + K\dot{\gamma}^n \quad (3)$$

$$\begin{aligned} \text{Bingham – Papanastasiou model } \tau \\ = \tau_0(1 - e^{-m\dot{\gamma}}) + \mu\dot{\gamma} \end{aligned} \quad (4)$$

$$\text{Casson model } \sqrt{\tau} = \sqrt{\tau_0} + \sqrt{\mu}\sqrt{\dot{\gamma}} \quad (5)$$

where, τ , τ_0 , μ , $\dot{\gamma}$, c , K , n , and m are the shear stress (Pa), yield stress (Pa), plastic viscosity (Pa.s), shear rate (s⁻¹), regression constant, consistency, power index, and regularisation parameter, respectively. Bingham model (Eq. 1) is commonly used for the characterisation of the rheological properties of cement pastes and the rest models (Eqs. 2–5) are used for a comparative study. The yield stress can be predicted from the all the models. Plastic viscosity can be estimated by (1), (2), (4), and (5). The rheological models were used for the curve fitting of the shear stress versus shear rate experimental data. Generally, standard error is calculated for all models to understand the relative level of correctness. The formula used for the determination of standard error (S_e) is shown in Eq. 6 [42].

$$S_e = 1000 \times \frac{\sqrt{\frac{\sum (X_e - X_m)^2}{n-2}}}{R} \quad (6)$$

Here, X_e , X_m , n , and R are the experimental value, value from rheological models, number of data points, and difference between the maximum and minimum experimental values.

4.2 Slump models

Rheological slump cone models proposed by Saak et al. [27], de Larrard et al. [28], Helmuth et al. [29], Roussel et al. [30], and Flatt et al. [31] to find the dimensionless slump (s') and dimensionless shear stress (τ') by inputting the mini-slump cone dimensional parameters. The analytical equations proposed by Saak et al. [27] can be given by Eqs. (7–9):

$$\tau' = \left(\frac{1}{6H_t} \right) \left[(h_o + h_t) - \frac{(h_t)^3}{(h_o + h_t)^2} \right] \quad (7)$$

$$s' = \left(\frac{s}{H_t} \right) = 1 - \left(\frac{h_o}{H_t} \right) - \left(\frac{h_1}{H_t} \right) \quad (8)$$

$$s = H_t - h_o - h_1 \quad (9)$$

where, s , H_t , h_o , h_t , and h_1 are the total slump height, the height of the slump cone, the distance from the top of slumped paste to the start of the slump flow, and the height of the slump flow [27]. Similarly, the dimensionless parameters proposed by de Larrard et al. [28] were provided by Eq. 10:

$$\tau' = \frac{1 - s'}{Ag} \quad (10)$$

where, A is the rheological fitting constant depending on the paste's apparent viscosity and shear stress, and g is the acceleration due to gravity. Later, Helmuth et al. [29] proposed a slump model based on the ASTM C143 slump cone [43] and Murtha's [44] force balance approach, which can be given by Eqs. 11 and 12:

$$\tau' = \left[\frac{(1 - s')}{6} \right] (R^2 + R + 1) \quad (11)$$

$$r_s = \sqrt{\left(\frac{28}{(1 - s')} - 3 \right)} - 1 \quad (12)$$

where, R and r_s are the ratio of the slump cone top diameter to the slumped diameter and radius of the slumped paste, respectively. Roussel et al. [30] derived an equation for the yield stress of cement paste considering the surface tension of the cement paste, and the relation can be given by Eq. 13.

$$\tau = 1.747 \rho V^2 r_s^{-5} - \lambda \frac{r_s^2}{V} \quad (13)$$

where, V , λ , and ρ_m are the volume of paste inside the slump cone, a coefficient which depends on the surface tension of the fluid and contact angle of the surface, specific gravity, respectively. For a wide range of tests, the author recommended the value of the coefficient (λ) to be 0.005 and approximately same for all cement mixes for any testing plane. The slump can be calculated from spread by using high workability slump flow concept proposed by Domone [45] as given by Eq. 14.

$$s = H_t - \frac{3V(r_s - r_t)}{\pi(r_s^3 - r_t^3)} \quad (14)$$

Here, r_t is the top radius of the slump cone. Later, Flatt et al. [31] proposed a simplified yield stress equation by correlating spread diameter with minimum yield stress between corrected Murata [46] and Roussel et al. [30] (considering surface tension) approaches. The equation is as shown in Eq. 15.

$$\tau = ae^{-br_s} \quad (15)$$

where, a and b are correlation coefficients and from the interpolation. The value of a and b are 8.1505 and -0.3506 , respectively.

5 Results

5.1 Mini-slump flow, marsh cone flow, and air content

Mini-slump flow, marsh cone flow, and air content of the pastes were measured as they represent fundamental workability of the fresh paste. The mini-slump flow test was used to measure the horizontal free flow of the lithium slag cement pastes in the absence of



obstacles. Again, the marsh cone flow was utilised to measure the efflux time to pass 1725 mL lithium slag cement paste through an 8 mm nozzle under gravity. The air content was measured to collect information on the volume of air contained within the lithium slag cement paste. The fresh mixes were tested according to the standard specifications, and the parameters were compared for various replacements of cement with lithium slag as given in Table 2. The changes in the air content, efflux time, and pat area of the 0–60% LS pastes are shown in Fig. 3h and a ternary plot of the normalised efflux time, pat area, and air content is

shown in Fig. 3i. All data were normalised to the results of the control mixture. The mini-slump pat area from each mix was determined from the image captured after the cone was lifted and analysed with the help of Jann5s MATLAB image processing program [47]. The air content and efflux time were recorded for each mix with appropriate moulds and standard procedure. The increasing volume of lithium slag in the cement paste reduced the pat area and air content while the efflux time increased as shown in Fig. 3h and i, respectively.

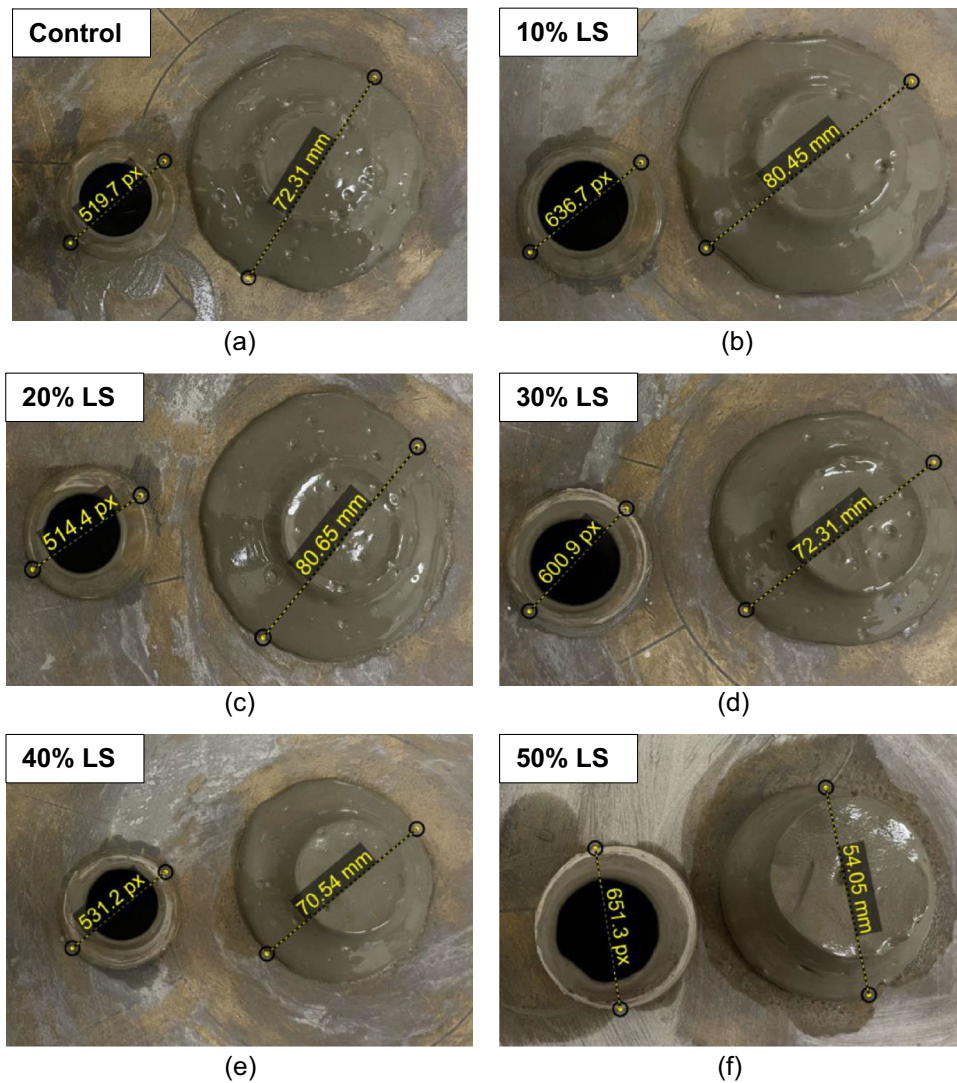


Fig. 3 Mini-slump pat diameter of 0–60% LS pastes at $w/b = 0.47$ (a–g), variation of air content, pat area, and efflux time with percentage contribution of lithium slag in the mixture

(h), and i ternary plot of normalised air content, pat area, and efflux time of 0–60% lithium slag cement fresh pastes

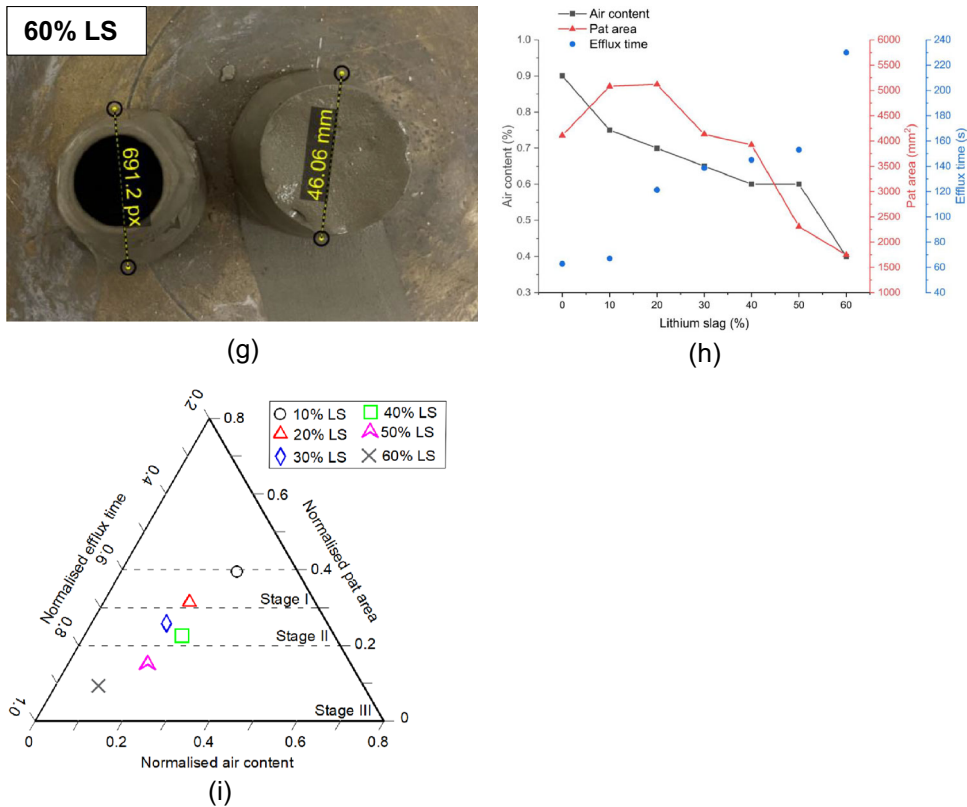


Fig. 3 continued

Many researchers have idealised the mini-slump test in various ways either through mathematical modelling of geometry [27], yield stress [32, 48], or flume test [49]. This study characterises the mini-slump flow of 0–60% lithium slag cement pastes through marsh cone flow value and air content. The mini-slump flow test was repeated for each mix and then averaged. The control specimen had a pat diameter of 72.31 mm, as shown in Fig. 3a. The pat diameter of the mixes was increased for 10–20% LS pastes followed by control, as shown in Fig. 3b and c, respectively. Later, the pat diameter consistently lowered for 30–60% LS pastes (Fig. 3d–f) and for 60% LS paste the reading was 46.06 mm, as shown in Fig. 3g. The variation of the mini-slump pat diameter with the increase of lithium slag percentage is given in Fig. 3h and the pat diameters were categorised into three stages based on the flowability of the control paste, as shown in Fig. 3i. In stage I (highly workable), the pat diameter of 10 and 20% LS was increased by 11.2% and 11.4% of the control. The mixes became highly workable as the void is reduced by the

combined particle packing of cement and lithium slag [50]. Later, in stage II (moderately workable), the pat diameter continuously decreased when LS replaced more than 30% cement. The pat diameter of the 40% LS mix was approximately equal to the control mix. This indicates that the particle grading and packing are optimum at 40% LS. Thus, a further cement replacement by lithium slag could not help increasing workability due to high particle porosity and internal surface area [21]. Moreover, an abrupt decrease in workability was recorded when the cement replacement was more than 40% as shown in the stage III (low workable) in Fig. 3h and i, respectively. As lithium slag particles being angular, flaky, and elongated, compromised the workability of the paste till 40% cement replacement for a constant w/b = 0.47. This also suggests that beyond 40% replacement, the water demand of the mix is relatively high to maintain similar workability of the pastes. As such, the mini-slump pat area was significantly reduced as illustrated in Fig. 3h-i.



Also, from Fig. 3h, the efflux time of lithium slag cement pastes decreased gradually with the increase of LS in the mix at a constant $w/b = 0.47$. The efflux time for water and the control cement paste was 8.07 and 62.75 s, respectively. The efflux time increased by approximately 7–267% for 10–60% LS mixes; the lower end margins are representative of lower LS substitutions. The flow of grout in the marsh cone and the air content of a paste depend on the shape, size, specific gravity and texture of particles, w/b ratio, and admixture content. The 60% LS paste lost the flowability and the slump shape was a frustum of a cone, as shown in Fig. 3g. Sathyan et al. [51] used different doses of admixture by lowering the cement mixture's water content and determine the saturation point through min-slump flow and efflux time. In Fig. 3h, the air content decreased with the increased lithium slag volume in the mixture. The air content of the control was 0.9% at a temperature 23 ± 1 °C. The drying-out phenomenon is also evident from the mixture's air content versus lithium slag content. The air content of 10–60% lithium slag cement pastes decreased by 17–56% compared to the control mix. Therefore, the slump flow of high-volume lithium slag cement paste decreased due to lowered air content, and the paste lost flowability.

5.2 Consistency and setting times

The variation of consistency and setting times of cement paste due to 0–60% LS pastes are shown in Fig. 4. The consistency and setting times of the 0–60% LS mixes were determined according to the standard procedure. The bar diagram indicates the change in the water consistency for 0–60% LS pastes. The water

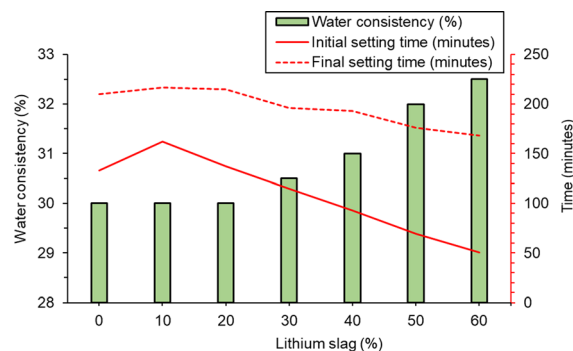


Fig. 4 Variation of water consistency and setting times with cement replaced by lithium slag at different proportion

consistency was slightly reduced for 10–20% lithium slag addition in the cement mixture, and the values were reported to the nearest 0.5% accuracy. The water consistency of 10–20% LS pastes was approximately 30 mm, similar to that of the control mix. In addition, the water requirement consistently increased for 30–60% LS pastes. The water consistency for 60% lithium slag paste was 32.5%. The standard water consistency of the cement depends upon the physical properties of the materials, such as specific surface area, size, texture, porosity, and shape, and the normal consistency of the cement should be 24–30% [52]. Lithium slag comprises irregular-shaped flaky particles (as depicted in Fig. 1), and the surface area increases at 30–60% LS mixes. Thus, the water requirement for 30–60% LS pastes increased to maintain the same consistency as the control.

The setting times of the mixes were determined, and findings are presented in Fig. 4. The setting times were measured at a temperature of 20 ± 1 °C with relative humidity $90 \pm 3\%$. The control mix's initial and final setting times were 133 min and 210 min, respectively. Interestingly, with the addition of high volume LS (beyond 20%), a significant reduction in the setting times were observed. The initial setting time of 10% and 20% LS mixtures was approximately increased by 22% and 3% compared to the control mix. In contrast, the initial setting time decreased by 14–62% in the pastes containing 30–40% LS pastes than the control. In general, the final setting can be correlated with the initial setting time based on ordinary Portland cement's test data, where final setting time (min) = $90 + 1.2 \times (\text{initial setting time})$ (min) [53]. The thumb rule overestimated the final setting time by 4–31% for 0–40% LS pastes but, however, underestimated the final setting times by 2–10% for 50–60% LS pastes.

A small addition of lithium slag ($\leq 10\%$) induced the setting times, and the difference is negligible compared to the control specimen [54]. The final setting time of 10% and 20% LS pastes were increased by 3% and 2%, respectively compared to the control. The water consistency of the 10–20% LS pastes was slightly lower than the control and adjusting 30% water consistency (0.5% accuracy) for 10–20% LS samples will yield slightly higher free surface water to induce the setting times. The alumina and sulfate content of lithium slag were higher than cement as listed in Table 1. At 10–20% cement replacement, the

alumina and sulfate were probably within the threshold limit for the setting of 10–20% LS pastes. The increased alumina and sulfate content of 30–60% LS pastes rapidly hydrated C_3S and decreases in the initial setting time [55]. The hydration of lithium slag cement pastes is discussed in Sect. 5.3.

5.3 Heat of hydration

The heat flow and cumulative heat of hydration generated per unit mass of the cement containing 0–60% lithium slag are shown in Figs. 5a and b, respectively. The hydration heat rate contains distinct phases of pure cement hydration despite the addition of LS, as shown in Fig. 5a. However, depending on the proportion of LS in the mix, temporal shifts in the occurrence of the phases were observed. Initially, a high heat release was observed for all mixes within 30 min generated from wetting and dissolution,

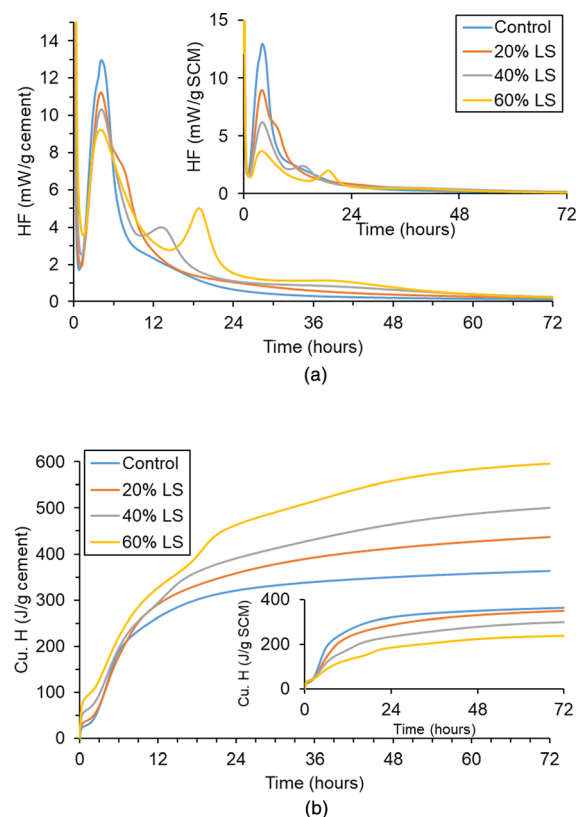


Fig. 5 Heat flow (a) and b cumulative heat of 0–60% LS paste with $w/b = 0.47$ expressed in terms of J/g cement and J/g SCM. Note “HF” represents heat flow and “Cu. H” is the cumulative heat



followed by a typical dormant period [56]. The dormant period indicates the formation of AFt by creating networks between the binder particles with the help of pore water. The dormant period is readily accelerated by the hydration of C_3S , and C_2S phases of cement to produce C–S–H [57], and this is captured in the formation of a peak within 5–6 h of hydration. A secondary peak, known as the sulfate depletion point, where the AFt phase converts into AFm phase by hydrating C_3A and C_4AF phases [58], is also observed in Fig. 5a. The aluminate and sulfate content of the composite system controls the secondary hydration reaction, and most importantly, the reactivity of the 20–60% LS pastes can be identified through the height and delayed appearance of the last peak [9, 59]. The secondary hydration phase is absent for the control, partly visible for 20% LS, and palpable for 40–60% LS pastes. The heat flow curve attains equilibrium after the AFm phase, and the steady state of heat flow is confirmed from the cumulative heat flow, as shown in Fig. 5b.

The heat flow of 0–60% lithium slag cement pastes provides essential information on the dormant, primary, and secondary hydration peaks. Although a higher concentration of lithium slag dilutes the clinker, and the dormant period was slightly prolonged, the initial setting time was significantly shortened for 40 and 60% LS pastes with respect to the control. This shift in setting time is also apparent in the heat flow curves where the secondary hydration peak (often referred to as the shoulder peak) becomes more prominent for higher LS replacements. The lithium slag contains 21.1% aluminium oxide, and a proportional increase in the aluminium was confirmed at higher replacements, which makes the pastes susceptible to flash sets due to the rapid hydration nature of alumina, much like the well-understood rapid setting of C_3A phase of cement. In essence, alkaline metals, silicates, carbonates, and aluminates hydrate the C_3A phase to produce enormous hydration heat and induce C_3S hydration to precipitate insoluble calcium ions with time. This is better understood in the cumulative heat curves of Fig. 5b where systems with higher proportion of slag resulted in greater heat releases.

However, the initial setting of 20% LS pastes was delayed by 4 min compared to the control paste, and the heat flow curves support this by marking the delayed dormant period. This shift in setting time and

the dormant period indicates that at lower replacement ratios, the alumina content is not high enough to cause the rapid reactions of such phases to induce setting and the dilution of clinker results in an increased workable time. However, beyond 20% replacement, the alumina content in the blend is the critical factor that controls setting.

The primary hydration peak is consistently reduced with an increased lithium slag content in the binary system. An increase in lithium slag content also increased the sulfate content but diluted the clinker, which is the primary source of C_3S and C_2S . Thus, the primary peak slumped consistently from the control and shifted slightly to the left. Besides, an abnormal increase in the slope of the cumulative heat curve of 40% and 60% lithium slag cement pastes was observed at approximately 12 and 18 h, respectively, as shown in Fig. 5b. The secondary peak of 20–60% LS pastes continuously increased as the aluminium and sulfate concentrations increased. The hydration heat of aluminate is higher than silicate, and a higher sulfate content in the lithium slag induces higher exothermic peaks and shifts the hydration curve to more right [60].

RILEM TC 267-TRM phase 3 [61] investigated the hydration heat generated by 13 slags, 10 fly ashes, and 10 natural pozzolans, from different sources and recommended a linear regression equation: $C_s =$

$0.095H_h - 39.13$ ($R^2 = 0.87$) for the prediction of relative compressive strength (C_s) from heat release (H_h) data. The study also categorized the relative compressive strength into three different categories such as: (i) unreactive (< -35), (ii) moderately reactive (-35 to 0), and (iii) highly reactive (> 0) and analysed the probability and prediction error through statistical methods. In this study, the hydration heat of 20, 40, and 60% LS pastes were 350, 300, and 238 J/g SCM, respectively, and the above regression equation predicts the relative compressive strength of 20–60% LS pastes to be moderately reactive. Specifically, the estimated average relative compressive strengths of 20, 40, and 60% LS pastes were -22.9 , -8.8 , -4.8 by considering the probability and prediction error for the regression equation. The hydration heat and the predicted relative strength of 60% LS paste were highly reduced than the control, followed by 40% and 20% LS pastes. Here, 40% LS was found to develop optimum for the hydration heat, and the estimated relative strength was also close to the 20% LS and control specimens.

5.4 Rheology

The rheology of the 0–60% lithium slag cement pastes were tested and expressed by shear stress versus shear rate curves, as shown in Fig. 6. In general, the

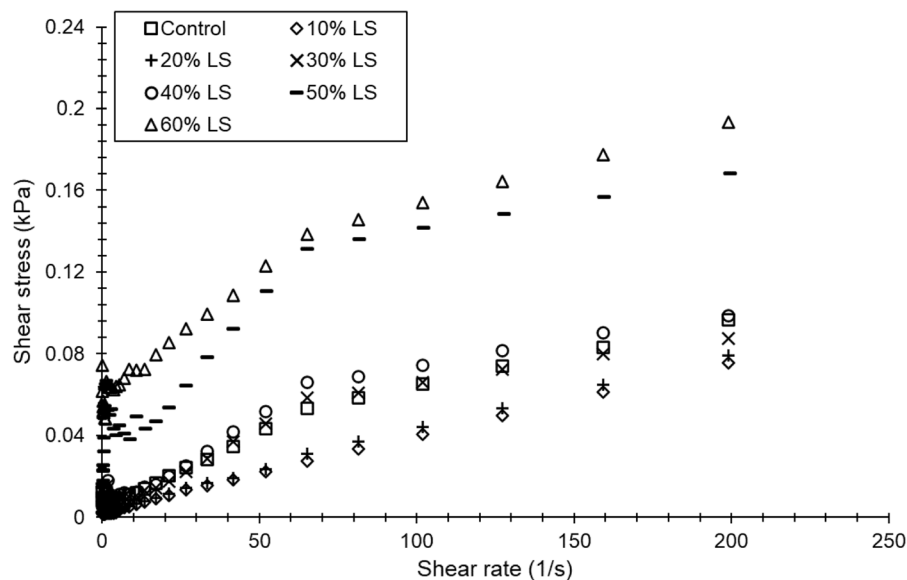


Fig. 6 Variation of the shear stress with shear rate for 0–60% LS pastes at $w/b = 0.47$

rheological behaviour of the pastes can be categorised into three distinct phases: (I) initial disturbance for the positioning rheometer geometry ($0\text{--}3\text{ s}^{-1}$), (II) unyielded immobilised paste under initial loading, and (III) yielded and plastic state of the paste [62]. In this experiment, the initial stress disturbance (phase I) of the cement paste was disregarded, as the zone did not influence the rheological behaviour of the lithium slag cement composite. Here, phases II and III were detected with increasing shear stress and shear rate curves. Rheology models [21, 23–26] were implemented to estimate the yield stress and plastic viscosity from the phases II and III which is discussed in the Sect. 6.2. In Fig. 6, the recorded shear stress of the control paste was 96.6 Pa at a shear rate 200 per second. The shear stress was highly reduced with an addition of 10–20% lithium slag as a SCM. The shear stress of 10% and 20% LS pastes was reduced by 22% and 18%, respectively than the control. The reduction of shear stress is due to the increased fluidity as depicted from the mini-slump pat diameter Fig. 3b and c, respectively. Interestingly, 30–60% lithium slag as a SCM increased the shear stress at same shear rate. The reduction of the mini-slump pat area of 30–60% LS pastes also reduced the fluidity from 72.31 to 46.06 mm, as shown in Fig. 3d to g. A 40% LS paste with $w/b = 0.47$ could produce a similar shear stress at same rate as control, while the mini-slump pat area was reduced by 2.5% than the control. Later, the shear stress of 50 and 60% LS pastes was increased by 74.5% and 100.5% than the control, as the mini-slump pat area was reduced by 25.3% and 36.3%, respectively in the same comparison. Lithium slag has a porous surface texture, and the high internal specific surface area adsorbs a high volume of water [11]. The irregular-shaped lithium slag possibly provided optimum packing for 10–20% LS pastes. The shear stress probably lowered for the increased fluidity and free surface water of 10–20% LS pastes. However, the flaky and irregular-shaped particles were increased for 30–60% LS pastes, and the pastes lost flowability. The free surface water of 30–60% LS pastes perhaps reduced for these pastes and the shear stress was increased.

5.5 Compressive strength

The compressive strength and strength activity index of 0–60% LS specimens at 7, 28, 56, and 180 days of

hydration are presented by the bar and scatter diagrams in Fig. 7. The strength activity index indicates the reactivity of 0–60% lithium slag in the cement pastes. At an early stage of hydration, the strength development of 10–60% LS pastes were lower than the control mix. In contrast, 10–30% LS pastes exhibited more highly reactive system to induce the compressive strength than the control at 28, 56, and 180 days. Also, the compressive strength development of 40–60% LS specimens significantly varied till 28 days. However, 40% LS improved strength development beyond 56 days. The difference in the strength reduction after 30% cement replacement was probably due to the fineness and chemical composition. The strength activity index of 10–50% LS pastes was more than 75%, and the compositions are considered to be acceptable in terms of strength development based on ASTM C618 [2] and AS/NZS 3582.1 [63]. Interestingly, 60% LS paste had a strength activity index greater than 65% on 180 days, confirming a moderately reactive system according to RILEM TC 267-TRM [61]. The reactivity of lithium slag derived from spodumene contained a higher concentration of SiO_2 and Al_2O_3 compared to cement and higher LOI in the same comparison. At high-volume cement replacement, the reactive silica and alumina induce the growth of the C-A-S-H phase, and better strength development is observed on 28 days of hydration [13]. The hydration heat and early strength development of the 0–60% LS pastes were proportionally reduced compared to the control. In general, the hydration heat of high alumina low calcium pozzolans reduces with the increase of cement replacement in the system [64, 65]. The early strength development is highly dependent on the hydration heat generated by the system, and temperature curing can replenish the heat difference to induce the pozzolanic activity of high volume low-calcium-high-alumina pozzolans [66]. Furthermore, temperature matched curing for high volume pozzolan (low-calcium-high-alumina) concrete could provide high early and long-term strength [66–68]. Therefore, increasing lithium slag (high alumina and low calcium) volume as a SCM seems to provide rapid hydration as observed in the setting and heat flow investigations, however, does not contribute to the early-age strength development due to lowered hydration heat generation.



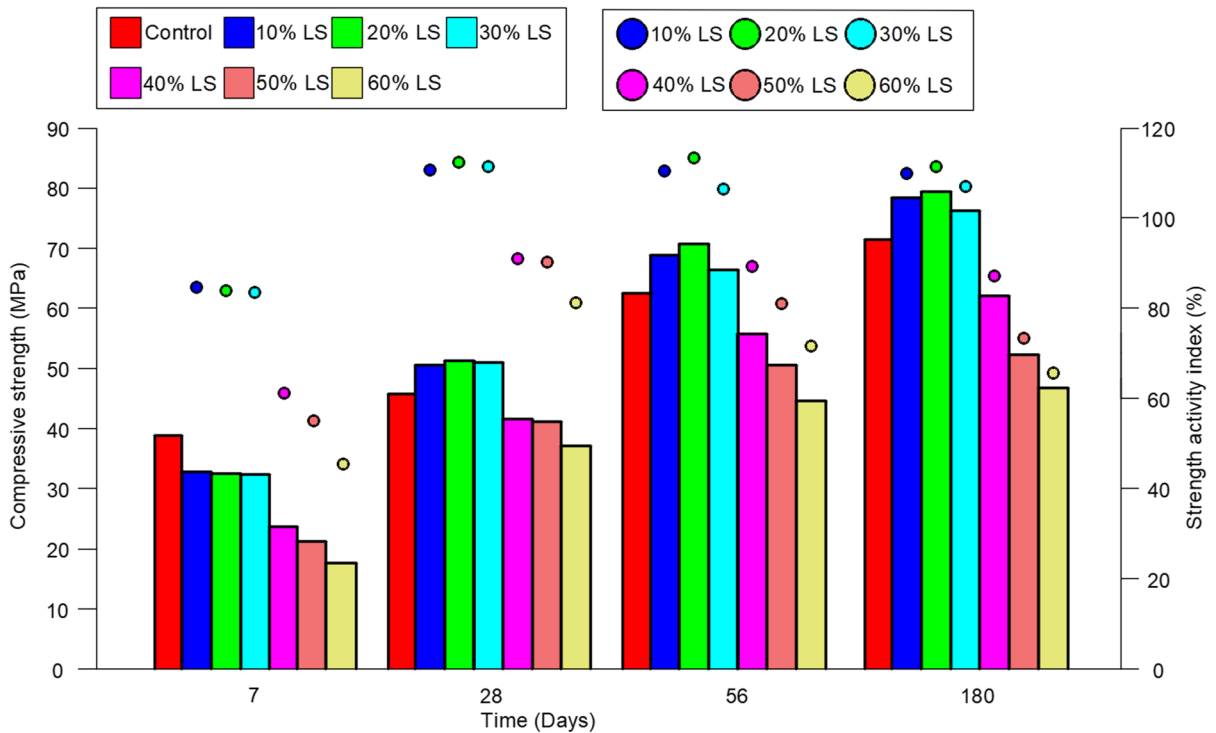


Fig. 7 Compressive strength and strength activity index of pastes with 0–60% lithium slag cement pastes at w/b = 0.47

6 Discussions

6.1 Correlation of maximum shear viscosity with air content, efflux time, and pat area

The correlations coefficients of air content, efflux time, and mini-slump pat area of 0–60% LS pastes with maximum shear viscosity are shown in Fig. 8. The R^2 values of air content, efflux time, and mini-slump pat area were 0.50, 0.64, and 0.96, respectively

for the prediction of maximum shear viscosity. Thus, the correlation coefficient of air content with the maximum shear viscosity is poor followed by marsh cone flow efflux time. Generally, air content is a fresh property of a paste but, it does not represent the flow behaviour of the system. The correlation coefficient is improved ($R^2 = 0.64$) for efflux time. Efflux time represents the time required to flow the paste under gravity, possibly unable to characterise the shear stress of parallel plate geometry, but may be effective for

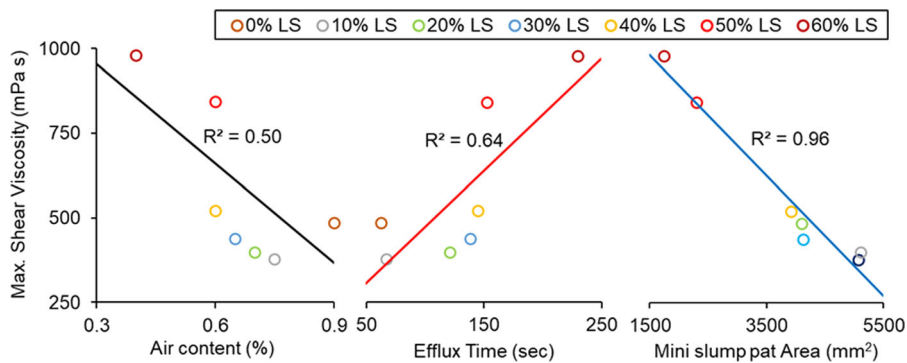


Fig. 8 Correlation coefficient of maximum shear viscosity with air content, marsh cone efflux time, and mini slump pat area for 0–60% LS pastes at w/b = 0.47



vane [27] and double cylinder viscometer [44]. In addition, the accuracy of the prediction of maximum shear viscosity by marsh cone flow rapidly decreases when the plastic viscosity is higher than 500 mPas [69]. In this study, the plastic viscosity of 40–60% LS pastes was higher than 500 mPas which reduced the correlation coefficient for efflux time. Alternatively, the correlation coefficient of mini-slump cone flow and maximum shear viscosity was 0.96, and the mini-slump flow data were found highly effective for the rheology characterisation of the lithium slag cement pastes. As mini-slump test contained small volume of pastes than the marsh cone and air content tests, the heterogeneity, test duration, and complexity of mini-slump test were low [69]. Therefore, the goodness of fit in the prediction of maximum shear viscosity by the pat area provided complete information for the flowability characterisation through parallel plate geometry [70]. In this study, classical rheology [21, 23–26] and slump models [27–31] will be discussed in Sects. 6.2 and 6.3 to characterise the rheology of 0–60% LS pastes.

6.2 Application of rheology models to determine the yield stress, plastic viscosity, and standard error

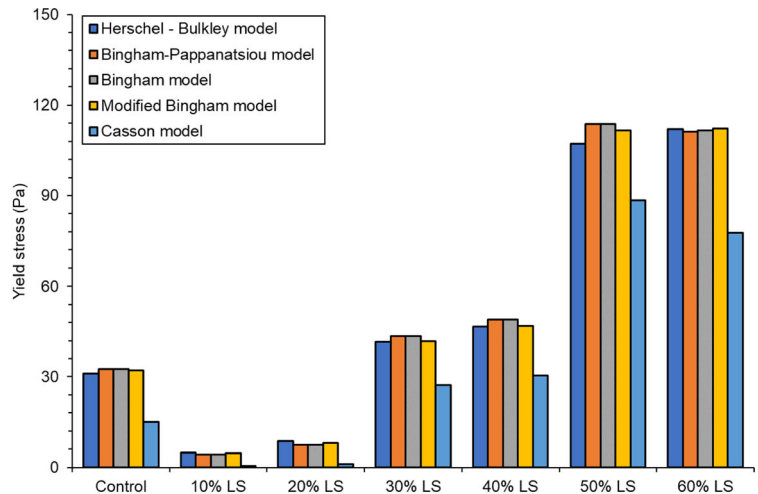
The estimated yield stresses from different rheological models [21, 23–26] of 0–60% LS pastes at $w/b = 0.47$ by using the parallel plate geometry are shown in Fig. 9a. The fresh mixes of 10% and 20% LS produced lower yield stress than control, but the yield stress proportionally increased with the cement replacement. Mostly, Casson model predicted lowest yield stress. This may be due to the underestimation of the shear at low shear rate by Casson model [42]. The yield stress predicted by Bingham-Papanastasiou model was similar to the Bingham model for 0–50% LS pastes. The prediction of yield stress through different rheology models were discretely ranked for all pastes and didn't follow any specific trend. In this study, Bingham and Bingham-Papanastasiou models predicted the highest yield stress for control and 30–50% LS pastes followed by the modified Bingham and Herschel-Bulkley models. In contrast, Herschel-Bulkley model predicted the maximum yield stress for 10, 20, and 60% LS pastes followed by modified Bingham model.

The rheology models were not significantly affected for the prediction of yield stress with the addition of lithium slag as a SCM due to smooth parallel plate geometry [42, 71].

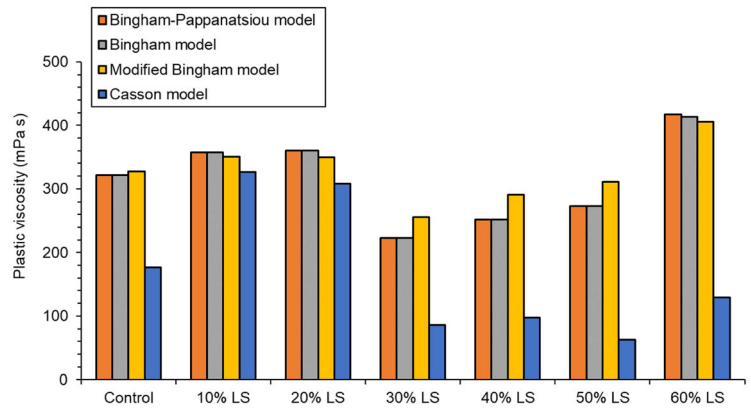
The plastic viscosity of 0–60% LS pastes (at $w/b = 0.47$) was estimated by Bingham, modified Bingham, Casson, and Bingham-Papanastasiou rheology models, as shown in Fig. 9b. The plastic viscosity was slightly increased for 10% LS paste than the control and unchanged for 20% LS. The plastic viscosity was highly dropped for 30% LS paste followed by a continuous increase for 40–60% LS pastes. For all pastes, Casson model estimated the lowest plastic viscosity. In contrast, the modified Bingham model predicted the highest plastic viscosity for control and 30–50% LS pastes. The Bingham and Bingham-Papanastasiou models predicted equal plastic viscosity for 0–50% LS pastes, and both models also estimated maximum plastic viscosity for 10–20% LS pastes, respectively. For 60% LS, Bingham-Papanastasiou rheology model predicted the highest plastic viscosity followed by Bingham and modified Bingham models.

In Fig. 9c, the standard error of different rheology models was plotted for the estimation of yield stress of 0–60% LS pastes. The standard error determined from the rheology models also did not follow a specific data trend for all fresh pastes. Generally, the standard error was lower for 10–20% LS pastes than all pastes. The standard error was highly increased for 30–40% LS pastes and then again reduced in the characterisation of 50–60% LS pastes. From Fig. 9c, the modified Bingham and Bingham rheology models were found feasible for the prediction of yield stress of 0–40% and 50–60% LS pastes based on least standard errors. Also, the standard error of Herschel-Bulkley model was lower than Bingham-Papanastasiou and Bingham models for 0–40% and 60% LS pastes, respectively. Casson model produced the maximum standard error for all pastes and unfeasible to use for the 0–60% LS pastes at $w/b = 0.47$. The performance of Casson rheological model consistently degrades with the increase of particles concentration in the cement paste suspension, as the model disregard the interaction between the phase particles in the hypothetical chains [72, 73].

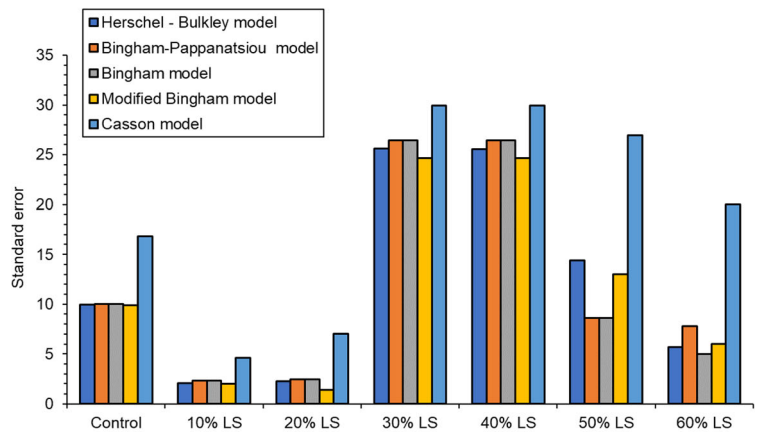
Fig. 9 Comparison of the predicted yield stress (a), plastic viscosity (b), and c standard error for 0–60% LS pastes at w/b = 0.47 for different rheological models [21, 23–26]



(a)



(b)



(c)

6.3 Application of slump models to determine the workable mixes

The slump and yield stress results of 0–60% cement replaced LS pastes with $w/b = 0.47$ recorded from the mini-slump cone and rheology tests. The slump flow and yield stress data were normalised using the Eqs. 16 and 17 [27], respectively.

$$s' = \frac{A_c}{f_a} \quad (16)$$

$$\tau' = \frac{\tau}{\rho_m g H_t} \quad (17)$$

where, A_c , f_a , and τ represents cone base area, slump flow area, and shear stress, respectively. In this study, the slump spread was continuously increased from the base diameter of the mini-slump cone (38 mm) to a finite value and the dimensionless yield stress was calculated for each slump models in a spread sheet. The analytical and experimental dimensionless slump versus dimensionless yield stress plotted in a same graph, as shown in Fig. 10.

The analytical models were proposed based on the mini-slump and shear stress produced by the fresh cement pastes at different w/b ratios. In this research, the analytical models will be used to idealise the extent of lithium slag that can be used as a SCM at $w/b = 0.47$. In Fig. 10, the variation of the dimensionless slump versus dimensionless shear stress of 0–40% LS pastes were close to the slump model proposed by Saak et al. [27], while 50–60% LS pastes can be interpreted by Hu and de Larrard [28], Roussel et al. [30], and Flatt et al. [31] slump models. There may have two possible reasons for which the

dimensionless slump and yield stress of 0–40% LS pastes were slightly underestimated from Saak et al. [27] model. Firstly, the experimental slump and yield stress of fresh 0–40% LS pastes were influenced by internal friction of the particles at an increasing shear rate. Secondly, the analytical slump models were developed based on the vane geometry but, the shear stress data of the pastes was quantified from smooth parallel plate geometry. Pierre et al. [74] pointed that the yield stress deviation between vane and parallel plate geometry increases with the increase of yield stress, plastic viscosity, and shear rate. In general, the efficiency of slump models is highly reduced at high shear mixing and the geometry of slump cone [27]. The experimental dimensionless shear stress and dimensionless slump of 50–60% LS pastes were highly deviated from Saak et al. [27] slump model. The experimental value of 50% LS was in between Hemuth et al. [29] and Hu and de Larrard [28] models, but very close to Flatt et al. [31] model. Besides, the dimensionless experimental slump of 60% LS paste was close to Roussel et al. [30] model followed by Flatt et al. [31] and Hu and de Larrard [28] models. The dimensionless slump of Roussel et al. [30] and Flatt et al. [31] slump models were calculated from Domone [45] slump flow model. Domone [45] primarily assumed the final shape of the slump to be a frustum of a cone during slump test for the establishment of slump flow model. In this study, the final slump of 50 and 60% LS fresh pastes was a cone frustum as depicted in Fig. 3f and g, respectively. Therefore, from Fig. 10, it is evident that the slump flow of 0–40% LS pastes with low yield stress can be interpreted by Saak et al. [27], as the deviation of shear stress is negligible compared to the control. Also, 50% and 60% LS pastes highly deviate from Hemuth et al. [29] and Hu and de Larrard [28] models, but rheology of the pastes can be effectively explained with Flatt et al. [31] and Roussel et al. [30] slump models. The surface tension of 50% and 60% LS pastes at $w/b = 0.47$ was probably played a dominant factor for the idealisation of slump model, which was only considered for Flatt et al. [31] and Roussel et al. [30] slump models. Thus, in this study, Flatt et al. [31] and Roussel et al. [30] analytical slump models are found to be feasible for high yield stress and plastic viscosity mixtures of 50–60% LS. These models can be used as alternative tools for the prediction of workability in

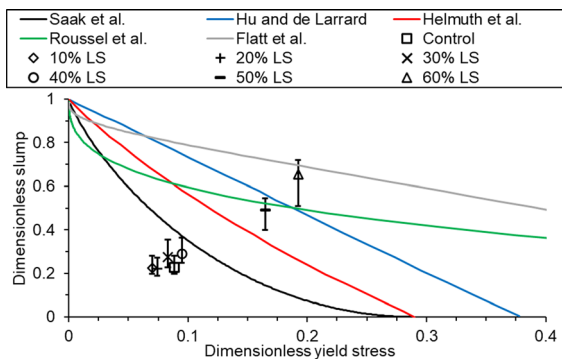


Fig. 10 Comparison of different slump models [27–31] with experimental data



comparison to the artificial neural network [75] and software modelling [76].

7 Conclusions

This study provides a comprehensive investigation of fresh properties and hydration heat evaluation of 0–60% lithium slag cement composites. The following conclusions can be drawn from the results and discussions:

1. A ternary plot of the normalised workability parameters could be used to categorise the workability of 0–60% lithium slag cement pastes at $w/b = 0.47$. Workability of the paste decreased with the increase of lithium slag content, specifically air content and slump flow decreased while the efflux time increased. This is attributed to the irregular and flaky shape of lithium slag particles. A 40% LS paste was found moderately workable in terms of mini-slump, marsh cone flow, and air content properties.
2. An increase in the lithium slag content also increases the water demand to produce a consistent paste. Though the density and specific surface area of lithium slag are less than those of cement, the excess water is required to fill up the pores of lithium slag. On the other hand, alumina and sulfate of lithium slag increase at high-volume cement replacement, which contributes to reducing the setting times. The setting times indicate that the 40% LS paste remained workable up to 90 min.
3. The total hydration heat per gram of cement increases with the increase of lithium slag in cement pastes. The higher cement replacement by lithium slag proportionately dilutes the clinker and lowers the main hydration peak. The increase in the aluminate and sulfate in high-volume lithium slag cement pastes induced a secondary hydration peak. A 40% LS paste can be idealised as a pozzolanic mixture as per RILEM TC 267-TRM phase 3 [61], generating 300 J/g SCM exothermic heat.
4. In addition, the control and 40% LS pastes produced approximately equal shear stress at the same shear rate at $w/b = 0.47$. The pastes containing more than 40% lithium slag became highly

viscous. A 40% LS paste holds a consistent strength development from early age to 180 days and provided 91% strength activity index on 28 days.

5. The mini-slump pat diameter produced the highest correlation ($R^2 = 0.96$) in the prediction of maximum shear viscosity of 0–60% LS pastes followed by the marsh cone flow efflux time and air content. The modified Bingham and Bingham rheology models produced the lowest standard errors in the prediction of yield stress and plastic viscosity of 0–40% and 50–60% LS pastes. The classical slump model of Saak et al. [27] was found feasible in the prediction of the slump of 10–40% LS pastes using the shear stress. The slump flow behaviour of 50% and 60% LS pastes can be idealised by Flatt et al. [31] and Roussel et al. [30] analytical slump models.

Acknowledgements This research was financially supported by the Australian Research Council (ARC)-DP200102784.

Funding Open Access funding enabled and organized by CAUL and its Member Institutions.

Open Access This article is licensed under a Creative Commons Attribution 4.0 International License, which permits use, sharing, adaptation, distribution and reproduction in any medium or format, as long as you give appropriate credit to the original author(s) and the source, provide a link to the Creative Commons licence, and indicate if changes were made. The images or other third party material in this article are included in the article's Creative Commons licence, unless indicated otherwise in a credit line to the material. If material is not included in the article's Creative Commons licence and your intended use is not permitted by statutory regulation or exceeds the permitted use, you will need to obtain permission directly from the copyright holder. To view a copy of this licence, visit <http://creativecommons.org/licenses/by/4.0/>.

References

1. Bekun FV et al (2022) Econometrics analysis on cement production and environmental quality in European Union countries. *Int J Environ Sci Technol* 20:4265–4280
2. ASTM C618 (2019) Standard Specification for Coal Fly Ash and Raw or Calcined Natural Pozzolan for Use in Concrete. American Society for Testing Materials: USA
3. Londono-Zuluaga D et al (2022) Report of RILEM TC 267-TRM phase 3: validation of the R3 reactivity test across a wide range of materials. *Mater Struct* 55(5):1–16



4. Talens Peiró L, Villalba Méndez G, Ayres RU (2013) Lithium: sources production uses and recovery outlook. *J Miner Metals Mater Soc TMS* 65(8):986–996
5. He Z et al (2020) Hydration and microstructure of concrete containing high volume lithium slag. *Mater Express* 10(3):430–436
6. Li J, Huang S (2020) Recycling of lithium slag as a green admixture for white reactive powder concrete. *J Mater Cycles Waste Manage* 22(6):1818–1827
7. Li J et al (2020) Recycling of lithium slag extracted from lithium mica by preparing white Portland cement. *J Environ Manage* 265:110551
8. Tan H et al (2020) Preparation for micro-lithium slag via wet grinding and its application as accelerator in Portland cement. *J Clean Prod* 250:119528
9. Zhang T et al (2020) Effect of TIPA on mechanical properties and hydration properties of cement-lithium slag system. *J Environ Manage* 276:111274
10. Tan H et al (2021) Effect of wet grinded lithium slag on compressive strength and hydration of sulphoaluminate cement system. *Constr Build Mater* 267:120465
11. Zhai M et al (2021) Hydration properties and kinetic characteristics of blended cement containing lithium slag powder. *J Build Eng* 39:102287
12. He Y et al (2022) Effects of TEA on rheological property and hydration performance of lithium slag-cement composite binder. *Constr Build Mater* 318:125757
13. Rahman SA, Shaikh FUA, Sarker PK (2022) A comprehensive review of properties of concrete containing lithium refinery residue as partial replacement of cement. *Constr Build Mater* 328:127053
14. He Z, Du S, Chen D (2018) Microstructure of ultra high performance concrete containing lithium slag. *J Hazard Mater* 353:35–43
15. Tan H et al (2018) Utilization of lithium slag by wet-grinding process to improve the early strength of sulphoaluminate cement paste. *J Clean Prod* 205:536–551
16. Li B et al (2019) Products and properties of steam cured cement mortar containing lithium slag under partial immersion in sulfate solution. *Constr Build Mater* 220:596–606
17. Haigh M et al. (2013) Development of New High Performance Supplementary Cementitious Material – A Lithium Production By-Product. In: *CIA Binnual Coference*. 2013, Concrete Institute of Australia (CIA): Australia
18. Munn B, Dumitru I, Maree D (2019) Assessment of the performance of new supplementary cementitious materials from lithium production residues. In: *CIA Binnual Coference*. 2019, Concrete Institute of Australia (CIA): Melbourne, Australia
19. Yin B et al (2018) Analysis of active ion-leaching behavior and the reaction mechanism during alkali activation of low-calcium fly ash. *Int J Concr Struct Mater* 12(1):50
20. Gartner E, Myers D (1993) Influence of tertiary alkanolamines on Portland cement hydration. *J Am Ceram Soc* 76(6):1521–1530
21. Herschel WH, Bulkley R (1926) Konsistenzmessungen von Gummi-Benzollösungen. *Kolloid-Zeitschrift* 39(4):291–300
22. He Z, Li L-Y, Du S (2017) Mechanical properties, drying shrinkage and creep of concrete containing lithium slag. *Constr Build Mater* 147:296–304
23. Bingham E (1922) Fluidity and plasticity. International chemical series. McGraw-Hill Book Compny Inc, New York
24. Yahia A, Khayat KH (2003) Applicability of rheological models to high-performance grouts containing supplementary cementitious materials and viscosity enhancing admixture. *Mater Struct* 36(6):402–412
25. Papanastasiou TC (1987) Flows of materials with yield. *J Rheol* 31(5):385–404
26. Casson N (1959) Flow equation for pigment-oil suspensions of the printing ink-type. *Rheol Disperse Syst: Conf Proc Br Soc Rheol* vii:84–104
27. Saak AW, Jennings HM, Shah SP (2004) A generalized approach for the determination of yield stress by slump and slump flow. *Cem Concr Res* 34(3):363–371
28. de Larrard F et al (1993) Design of a rheometer for fluid concretes. *Bull liaison lab ponts chaussees* 186:55–59
29. Helmuth RA, Hills LM, Whiting DA, Bhattacharja S (2006) Abnormal concrete performance in the presence of admixtures, Report 2006, Portland Cement Association, Skokie, IL, USA
30. Roussel N, Stefani C, Leroy R (2005) From mini-cone test to Abrams cone test: measurement of cement-based materials yield stress using slump tests. *Cem Concr Res* 35(5):817–822
31. Flatt RJ, Larosa D, Roussel N (2006) Linking yield stress measurements: spread test versus Viskomat. *Cem Concr Res* 36(1):99–109
32. Tan Z, Bernal SA, Provis JL (2017) Reproducible mini-slump test procedure for measuring the yield stress of cementitious pastes. *Mater Struct* 50(6):235
33. ASTM C138/138M. (2017) Standard Test Method for Density (Unit Weight), Yield, and Air Content (Gravimetric) of Concrete
34. ASTM C939/C939M (2016) Standard Test Method for Flow of Grout for Preplaced-Aggregate Concrete (Flow Cone Method). American Society for Testing Materials USA
35. ASTM C 187. (2016) Standard Test Method for Amount of Water Required for Normal Consistency of Hydraulic Cement Paste. American Society for Testing Materials: USA
36. ASTM C403/C403M. (2016) Standard Test Method for Time of Setting of Concrete Mixtures by Penetration Resistance. American Society for Testing Materials: USA
37. ASTM C138/C138M. (2017) Standard Test Method for Density (Unit Weight), Yield, and Air Content (Gravimetric) of Concrete. 2017, American Society for Testing Materials: USA. p 1–6
38. Mukhopadhyay AK, Jang S (2012) Predicting cement-admixture incompatibilities with cement paste rheology. *Transp Res Rec* 2290(1):19–29
39. ASTM C109/C109M. (2020) *Standard Test Method for Compressive Strength of Hydraulic Cement Mortars (Using 2-in. or [50 mm] Cube Specimens)*. American Society for Testing Materials USA.
40. AS 1012.8. (2014) *Methods of testing concrete Method for making and curing concrete - Compression and indirect tensile test specimens*. Australian Standard: Australia



41. Jeong J, Ramézani H, Chuta E (2019) Reactive transport numerical modeling of mortar carbonation: atmospheric and accelerated carbonation. *J Build Eng* 23:351–368
42. Nehdi M, Rahman MA (2004) Estimating rheological properties of cement pastes using various rheological models for different test geometry, gap and surface friction. *Cem Concr Res* 34(11):1993–2007
43. ASTM C143. (1978) Standard Test Method for Slump Of Portland Cement Concrete. American Society for Testing Materials USA.
44. Murata J (1984) Flow and deformation of fresh concrete. *Matériaux et Construction* 17(2):117–129
45. Domone P (1998) The slump flow test for high-workability concrete 11Communicated by C. D. Pomeroy. *Cem Concr Res* 28(2):177–182
46. Chamberlain J et al (2003) Experimental validation of incipient failure of yield stress materials under gravitational loading. *J Rheol* 47(6):1317–1329
47. Neggers J (2023) *Jann5s/measuretool*. <https://github.com/Jann5s/measuretool> [2.1.0.0]
48. Mukhopadhyay AK, Jang S (2012) Predicting cement-admixture incompatibilities with cement paste rheology. *Transp Res Rec J Transp Res Board* 2290(1):19–29
49. Gao J, Fourie A (2015) Using the flume test for yield stress measurement of thickened tailings. *Miner Eng* 81:116–127
50. Mehdipour I, Khayat KH (2017) Effect of particle-size distribution and specific surface area of different binder systems on packing density and flow characteristics of cement paste. *Cement Concr Compos* 78:120–131
51. Sathyan D, Balakrishnan AK, Mohandas SM (2018) Temperature influence on rheology of superplasticized pozzolana cement and modeling using RKS algorithm. *J Mater Civ Eng* 30(9):04018221
52. ASTM C187. (2016) Standard Test Method for Amount of Water Required for Normal Consistency of Hydraulic Cement Paste. American Society for Testing Materials: USA
53. Neville AM (2012) *Properties of Concrete*, 5th edn. Pearson Inc., UK
54. da Silva WRL, Šmilauer V, Štemberk P (2015) Upscaling semi-adiabatic measurements for simulating temperature evolution of mass concrete structures. *Mater Struct* 48(4):1031–1041
55. Zunino F, Scrivener K (2022) The influence of sulfate addition on hydration kinetics and C-S-H morphology of C3S and C3S/C3A systems. *Cem Concr Res* 160:106930
56. Mahmood AH et al (2022) The efficiency of recycled glass powder in mitigating the alkali-silica reaction induced by recycled glass aggregate in cementitious mortars. *Mater Struct* 55(6):156
57. Bullard JW et al (2011) Mechanisms of cement hydration. *Cem Concr Res* 41(12):1208–1223
58. Ylmén R, Wadsö L, Panas I (2010) Insights into early hydration of Portland limestone cement from infrared spectroscopy and isothermal calorimetry. *Cem Concr Res* 40(10):1541–1546
59. De Schutter G (1999) Hydration and temperature development of concrete made with blast-furnace slag cement. *Cem Concr Res* 29(1):143–149
60. Zunino F, Scrivener K (2020) Factors influencing the sulfate balance in pure phase C3S/C3A systems. *Cem Concr Res* 133:106085
61. Londono-Zuluaga D et al (2022) Report of RILEM TC 267-TRM phase 3: validation of the R3 reactivity test across a wide range of materials. *Mater Struct* 55(5):142
62. Jeong J et al (2020) Rheological properties for fresh cement paste from colloidal suspension to the three-element Kelvin-Voigt model. *Rheol Acta* 59(1):47–61
63. AS/NZS 3582.1. (2016) Supplementary cementitious materials in Part 1: Fly ash. , Australian Standard: Australia. p 16
64. Nguyen H-A et al (2019) Influence of low calcium fly ash on compressive strength and hydration product of low energy super sulfated cement paste. *Cement Concr Compos* 99:40–48
65. Thomas M (2007) Optimizing the use of fly ash in concrete. Portland Cement Association, Skokie
66. Bamforth P and BS (1980) In situ measurement of the effect of partial portland cement replacement using either fly ash or ground granulated blast-furnace slag on the performance of mass concrete. *Proc Inst Civ Eng.* 69(3): 777–800.
67. Neville AM (1995) *Properties of concrete*. Longman, London
68. Thomas M (2013) *Supplementary cementing materials in concrete*. CRC Press, Boca Raton
69. Le Roy R, Roussel N (2005) The marsh cone as a viscometer: theoretical analysis and practical limits. *Mater Struct* 38(1):25–30
70. Mukhopadhyay AK, Jang S (2009) Using cement paste rheology to predict concrete mix design problems: technical report. 2009, Texas Transportation Institute, The Texas A&M University System: USA
71. Yahia A, Khayat KH (2001) Analytical models for estimating yield stress of high-performance pseudoplastic grout. *Cem Concr Res* 31(5):731–738
72. Atzeni C, Massidda L, Sanna U (1985) Comparison between rheological models for portland cement pastes. *Cem Concr Res* 15(3):511–519
73. Papo A (1988) Rheological models for cement pastes. *Mater Struct* 21:41–46
74. Pierre A et al (2017) A study on the limitations of a vane rheometer for mineral suspensions using image processing. *Rheol Acta* 56(4):351–367
75. Yeh IC (2007) Modeling slump flow of concrete using second-order regressions and artificial neural networks. *Cement Concr Compos* 29(6):474–480
76. Bouvet A, Ghorbel E, Bennacer R (2010) The mini-conical slump flow test: analysis and numerical study. *Cem Concr Res* 40(10):1517–1523

Publisher's Note Springer Nature remains neutral with regard to jurisdictional claims in published maps and institutional affiliations.

